INTERNATIONAL SOCIETY FOR SOIL MECHANICS AND GEOTECHNICAL ENGINEERING

Characteristics on liquefaction behavior of undisturbed sample subjected to aging effect

Caractéristiques du comportement de liquéfaction de l'échantillon non perturbé soumis à l'effet de vieillissement

Tsuyoshi Honda & Natsuki Adachi
Research & Development Institute, Takenaka Corporation, Japan, honda.tsuyoshi@takenaka.co.jp

ABSTRACT: Undrained cyclic triaxial tests using high-quality undisturbed specimens were conducted to assess liquefaction resistance for sand with fines and gravel subjected to aging effects. The specimens were collected from the Pleistocene layer with an N-value of approximately 10 and a shear wave velocity of 180 m/s. A new method for calculating a liquefaction strength curve from one specimen using a concept of cumulative dissipation energy was adopted, and the intrinsic dispersion of the liquefaction resistance for the natural sedimentary sand was studied by comparing the liquefaction behavior of two specimens. The results showed that the difference between two specimens in liquefaction resistance was approximately 1.5 times. In addition, the dynamic properties of the equivalent shear modulus and damping ratio were calculated from the stress-strain loops for the seismic response analysis. It was observed that the damping ratio at a shear deformation of about 0.2% was twice as high as in conventional tests for dynamic deformation properties. The reason for this is that sand with fines subjected to aging effects had a low phase angle.

RÉSUMÉ : Des essais triaxiaux cycliques non drainés utilisant des spécimens non perturbés de haute qualité ont été effectués pour évaluer la résistance à la liquéfaction du sable avec des fines et du gravier soumis à des effets de vieillissement. Les échantillons ont été prélevés dans la couche de Pléistocène avec une valeur N d'environ 10 et une vitesse d'onde de cisaillement de 180 m/s. On a adopté une nouvelle méthode pour calculer une courbe de résistance à la liquéfaction à partir d'un spécimen en utilisant un concept d'énergie de dissipation cumulative, et on a étudié la dispersion intrinsèque de la résistance à la liquéfaction pour le sable sédimentaire naturel en comparant le comportement de liquéfaction de deux spécimens. Les résultats ont montré que la différence entre deux spécimens dans la résistance à la liquéfaction était d'environ 1,5 fois. De plus, les propriétés dynamiques du module de cisaillement équivalent et du rapport d'amortissement ont été calculées à partir des boucles contrainte-déformation pour l'analyse de la réponse sismique. On a observé que le rapport d'amortissement à une déformation de cisaillement d'environ 0,2 % était deux fois plus élevé que dans les essais conventionnels pour les propriétés de déformation dynamique. La raison en est que le sable avec des fines soumises à des effets de vieillissement avait un angle de phase faible.

KEYWORDS: aging effect, cumulative dissipation energy, liquefaction, liquefaction strength curve, shear wave velocity.

1 INTRODUCTION

Ground motions for structures' design had been increasing with a recent advance in seismic observation records. Even in the case of ground liquefaction, areas and strata with a liquefaction safety factor of less than 1.0 have been expanded using the conventional method based on N-values and fine fraction content due to the increase of ground motion. Although liquefaction occurred over a wide area in the 2011 off the Pacific coast of Tohoku Earthquake, the areas where serious damage occurred were concentrated in reclaimed lands and soft ground along rivers with relatively new sedimentation ages (Yasuda et al. 2012), and no serious damage occurred in reclaimed lands and natural ground formed several 100 years ago, which indicated influence of aging effects on liquefaction strength (Towhata et al. 2014).

In this paper, high-quality undisturbed samples were collected from Pleistocene sand with fines and gravel by 'Gel-Push' (GP) sampling (Taylor et al. 2012) and undrained cyclic triaxial tests were carried out to develop a more rational evaluation method for liquefaction resistance. In addition, a liquefaction strength curve was obtained from the result of one specimen using the concept of cumulative dissipation energy (Honda & Shigeno 2017, Honda et al. 2020). Next, we focused on the changes in the shear strain, shear stiffness and damping ratio during liquefaction to evaluate the physical properties used in the effective stress analysis. As a result, it was observed that the damping ratio showed very large value until 0.2% in shear strain, and then gradually decreased from 18% to 10% over the range from 0.2% to 2%.

2 UNDRAINED CYCLIC TRIAXIAL TESTS

The object soil layer is sand with fines and gravel at GL -10 m with an N-value of about 10 and S-wave velocity of 180 m/s. The geological age is Pleistocene and is just below the lower part of the Holocene sandy soil. No method for quantitatively evaluating aging effects of soil has been established, but the collected sand was assumed to be influenced by the aging effects from the sedimentary age. Undisturbed samples with a diameter of 100 mm were collected by GP sampling using polymer solution instead of circulating water. Figure 1 shows the schematic method for GP sampling. The sample collected GP sampling is shown in Figure 2. It was found that the sample has enough strength and hardness to stand on its own and that the sandy soil retained some cementation.

Undrained cyclic triaxial tests were carried out using two specimens (GP-10-1 and GP-10-2) selected from the sample of about 900 mm in length. The specimen sizes were 100 mm and 200 mm in diameter and height respectively. Consolidation process was carried out using the mean effective principal stress of 70 kN/m^2 as the isotropic confining pressure, σ'_c that was calculated from the overburden pressure and a static earth pressure coefficient, K0 of 0.5. After the consolidation, P and S-wave velocities in the triaxial cell were measured using piezoelectric accelerometers (Tanaka & Yamada 2015), and then the undrained cyclic load tests were continued until liquefaction occurred while increasing the cyclic stress ratio in order of 0.036

(1st - 2nd cycles), 0.075 (3rd - 4th cycles), 0.150 (5th - 6th cycles), and 0.280 (after 7th cycles). The reason why the cyclic stress ratio was gradually increased is to obtain the number of cycles for a wide range of cyclic stress ratio in calculating a liquefaction strength curve using the concept of cumulative dissipation energy (Honda et al. 2020).
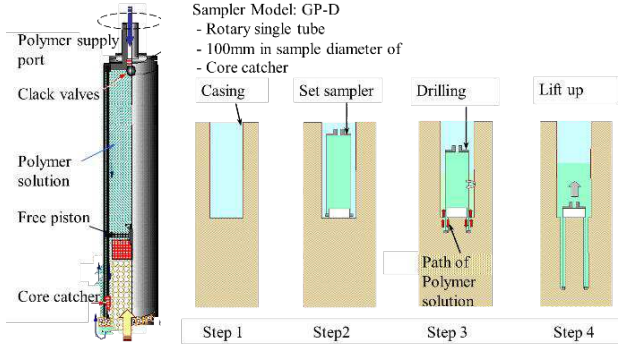

Figure 1. Procedures of 'Gel-Push' sampling using polymer solution instead of circulating water.
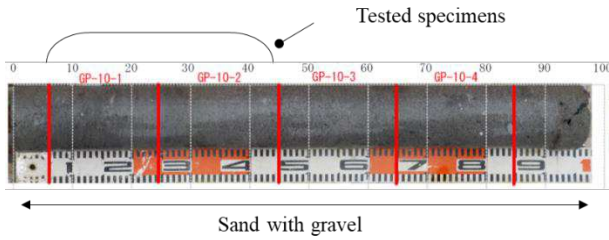

Figure 2. A photograph of collected sample using GP sampling.

Table 1. Specifications and results for the tested specimens.

Soil classification	Sand with gravel	
Test No.	GP-10-1	GP-10-2
Fines (%)	32.2	25.1
Clay (%)	9.1	6.2
Maximum grain size (mm)	9.5	19
Mean grain size, D_{50} (mm)	0.249	0.324
Maximum void ratio, e_{max}	1.136	1.144
Minimum void ratio, e_{min}	0.568	0.587
Relative density, D_r (%)	99.3	94.1
In-situ P-wave velocity, V_p (m/s)	1420	
In-situ S-Wave velocity, V_s (m/s)	180	
Effective overburden pre., (kN/m^2)	103.0	
Mean effective principal stress (kN/m^2)	68.7	
Isotropic confining pre., (kN/m^2)	70.0	70.0
P-wave velocity in Lab., V_p (m/s)	1720	1720
S-wave velocity in Lab., V_s (m/s)	218	199
Maximum CSR, τ_{max}/σ'_c	0.28	0.28
Number of cycles at $\Delta u/\sigma'_c$ = 0.95	64	32
Number of cycles at DA = 5%	125	101
RL_{20}	0.520	0.355

Table 1 shows the physical properties in each specimen, the P and S-wave velocity in the triaxial cell and the numbers of cycles at the excess pore water pressure ratio $\Delta u/\sigma'_c$ = 0.95 and the double amplitude strain DA = 5%. Here, the number of cycles indicates that during the maximum cyclic stress ratio of 0.280 (Not counted to the sixth cycle). Although the two specimens were collected from the almost same depth, the fine fraction content varied from 25 % to 32 %. The relative density was very

high due to influence of fine content, though the N-values were around 10. Figure 3 illustrates grain size distribution curves of the two specimens.

P-wave velocity in the triaxial cell was higher than in situ because the back pressure was twice higher than the in-situ water pressure. On contrary, S-wave velocity was almost the same value. The same S-wave velocity indicated that the collected sample had a good quality. In the undrained cyclic triaxial tests, the difference of 2 times in the number of cycles was induced at the excess pore water pressure ratio of 0.95, which is the initial liquefaction, and at double amplitude strain of 5%, which is considered to be the complete liquefaction.
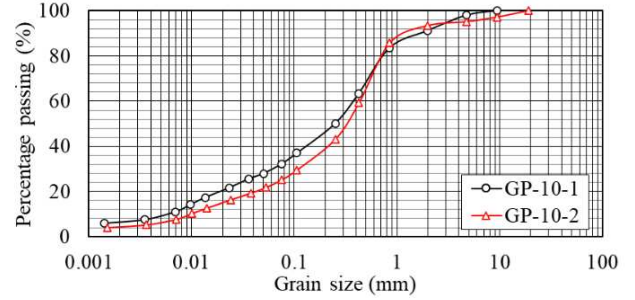

Figure 3. Grain size distribution curves for two specimens.

3 RESULTS & DISCUSSION

Figures 4 and 5 show the stress-strain relationship and stress path of GP-10-1 and GP-10-2 respectively. In these figures, the shear stress τ, the shear strain γ and the mean effective principal stress p' were calculated from the axial stress σ'_a and the axial strain ε_a, the radial stress σ'_r and the radial strain ε_r in the cyclic triaxial tests by the following equations.

$$\tau = q/2 = \left(\sigma_a - \sigma_r \right)/2 \tag{1}$$

$$\gamma = \varepsilon_a - \varepsilon_r = 1.5\varepsilon_a \tag{2}$$

$$p' = \left(\sigma'_a + 2\sigma'_r \right)/3 \tag{3}$$

where q is a deviator stress. In these stress paths, the rupture lines show the condition that the excess pore pressure ratio reached 0.95, which was derived from the equation of $\sigma'_r = \sigma'_c - \Delta u = 0.05 \ \sigma'_c$. The failure and phase lines for cohesive sandy soil are obtained from Mohr-Coulomb's failure criteria and the following relationships in the triaxial tests,

$$\sigma'_1 = \frac{2c'\cos\phi'}{1-\sin\phi'} + \frac{1+\sin\phi'}{1-\sin\phi'}\sigma'_3 \tag{4}$$

$$\pm q = \sigma'_1 - \sigma'_3 = \frac{2c'\cos\phi'}{1-\sin\phi'} + \frac{2\sin\phi'}{1-\sin\phi'}\sigma'_3 \tag{5}$$

$$p' = \frac{\left(\sigma'_1 + 2\sigma'_3\right)}{3} = \frac{1}{3} \times \left(\frac{2c'\cos\phi'}{1-\sin\phi'} + \frac{3-\sin\phi'}{1-\sin\phi'}\sigma'_3 \right) \ (com.) \tag{6}$$

$$p' = \frac{\left(2\sigma'_1 + \sigma'_3\right)}{3} = \frac{1}{3} \times \left(\frac{4c'\cos\phi'}{1-\sin\phi'} + \frac{3+\sin\phi'}{1-\sin\phi'}\sigma'_3 \right) \ (ext.) \tag{7}$$

where σ'_1 and σ'_3 are the maximum and minimum principal stress respectively, c' and ϕ' is cohesion and friction angle. Eqs. 6 and 7 show the mean effective principal stress in compression and extension mode respectively. The failure lines illustrated in Figures 4 and 5 is obtained from the following equations,
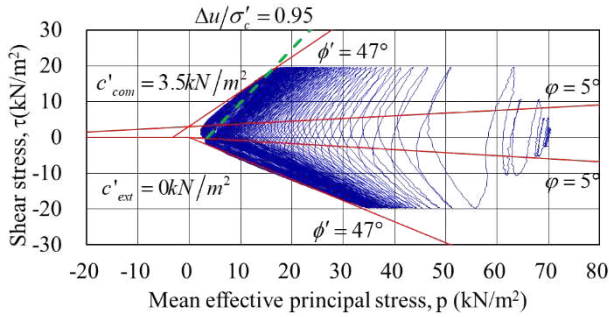
100

$$\tau = \frac{3\sin\phi'}{3 - \sin\phi'} \times \left(p' - \frac{2c'\cos\phi'}{3 - 3\sin\phi'} \right) + \frac{c'\cos\phi'}{1 - \sin\phi'} \quad (com.) \qquad (8)$$

$$\tau = -\frac{3\sin\phi'}{3 + \sin\phi'} \times \left(p' - \frac{4c'\cos\phi'}{3 - 3\sin\phi'} \right) - \frac{c'\cos\phi'}{1 - \sin\phi'} \quad (ext.) \qquad (9)$$

The phase lines are also obtained by using the phase angle φ instead of the friction angle ϕ' as in Figures 4 and 5.
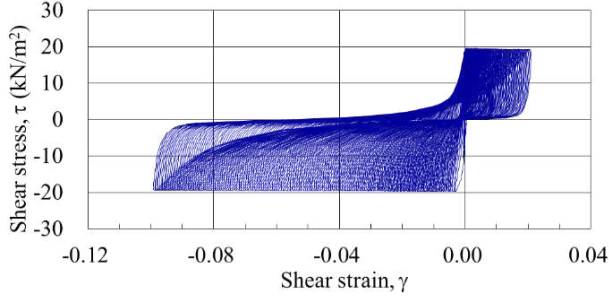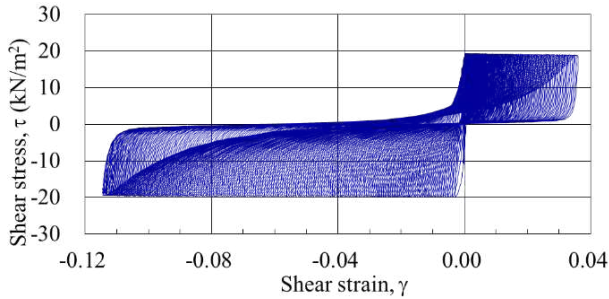

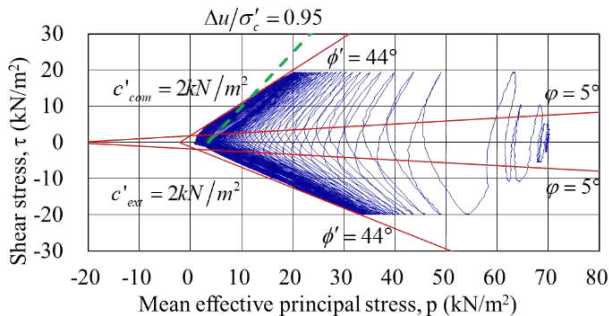(a) Relationship between shear stress and shear strain

(b) Stress path

Figure 4. Results in undrained cyclic triaxial test in GP-10-1

(a) Relationship between shear stress and shear strain

(b) Stress path

Figure 5. Results in undrained cyclic triaxial test in GP-10-2

From the stress paths in Figures 4 and 5, it was found that the collected sample from the Pleistocene layer had some cohesion and large friction angle even if the N-value was not large. The most remarkable characteristic for the Pleistocene layer is the very low phase angle. In other words, the specimens from the Pleistocene layer show intensive cyclic mobility.

The dissipation energy in one cycle of loads, ΔU and the cumulative dissipation energy until the end of n-th cycle, U_n were calculated from Eqs. 10 and 11.

$$\Delta U = \int \tau \cdot d\gamma \qquad (10)$$

$$U_n = \sum_{i=1}^{n} \Delta U \qquad (11)$$

where $d\gamma$ is the increment of shear strain. Normalizing the cumulative dissipation energy, U_n and the shear stress, τ_{max} by the effective confining pressures at the end of n-th cycle, $_{n+1}\sigma'_c$, two particular relationships are obtained (Honda et al. 2020). One is the relationship between the normalized dissipation energy, $U_n/_{n+1}\sigma'_c$ and excess pore pressure ratio, $\Delta u/\sigma'_c$. The other is the relationship between the increment of the normalized cumulative dissipation energy, $\Delta(U_n/_{n+1}\sigma'_c)$ obtained from Eq. 12 and the shear stress ratio, $\tau_{max}/_n\sigma'_c$.

$$\Delta\left(\frac{U_n}{_{n+1}\sigma'_c} \right) = \frac{U_n}{_{n+1}\sigma'_c} - \frac{U_{n-1}}{_n\sigma'_c} \qquad (12)$$

Figure 6 shows the relationships between the normalized cumulative dissipation energy and the maximum excess pore water pressure ratio at each cycle. Honda and Shigeno (2017) and Honda et al. (2020) conducted liquefaction strength tests using the reconstituted specimens and found that the relationships coincided on the same curve even if the cyclic stress ratio was changed. Now, the same cyclic stress ratio was used for the two specimens. Therefore, the difference between the two specimens was caused by the dispersion of the ground.
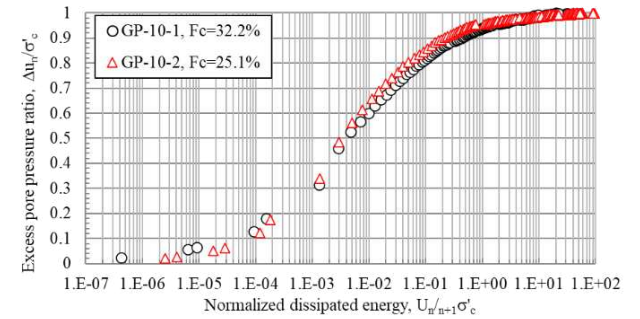

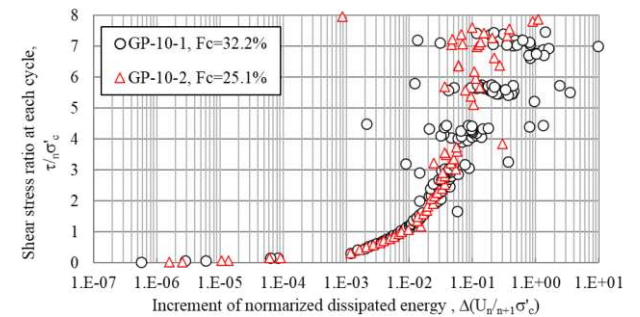Figure 6. Relationship of normalized dissipation energy and excess pore pressure ratio.

Figure 7. Relationships of shear stress ratios and increments of normalized cumulative dissipation energy.

Figure 7 shows the relationship between the increment of normalized cumulative dissipation energy and the cyclic shear stress of each cycle divided by the effective confining pressure $_n\sigma'_c$ at the beginning of the n-th cycle. In these tests, the amplitude

of shear stress was kept constant from the 7th cycle, but the cyclic stress ratio divided by the effective confining pressure at the beginning of each cycle increased, since the excess pore water pressure increased. In addition, it was also confirmed that the relationships in Figure 7 are coincided on the same curve regardless of the cyclic stress ratio (Honda & Shigeno 2017, Honda et al. 2020). Here, when the cyclic stress ratio of each cycle exceeded about 2.0, the scatter of the data became very large. The reason for this is thought to be that the effective confining pressure at the end of the cycle approached zero, and that excess pore water pressure and shear strain for a dense sand not always increased every cycle of loading, but they increased after multiple cyclic loads were applied.

Comparing the two specimens in Figures 6 and 7, the GP-10-2 had a larger excess pore water pressure ratio with respect to the same normalized cumulative dissipation energy, and a larger increment of the normalized cumulative dissipation energy with respect to the same cyclic stress ratio. This is consistent with the fact that the GP-10-2 had a lower liquefaction resistance than the GP-10-1 because of its lower fine fraction content, relative density, and S-wave velocity.

Next, the liquefaction strength curves were calculated using the relationship between Figures 6 and 7. In practice, the relationship between the excess pore water pressure ratio ($1 - {}_{n+1}\sigma'_c/\sigma'_c$) at the beginning of the n+1 cycle, which meant at the end of n cycle, and the normalized cumulative dissipation energy was prepared as in Figure 8.

Figure 9 shows the flow chart to calculation liquefaction strength curve using one undrained cyclic triaxial test. The liquefaction strength curve is determined by the following procedures,

(1) An arbitrary cyclic shear stress amplitude τ and an effective confining pressure σ'_c (= ${}_1\sigma'_c$) are set.
(2) From the cyclic stress ratio $\tau/{}_n\sigma'_c$ at the n-th cycle, the increment of normalized cumulative dissipation energy $\Delta(U_n/{}_{n+1}\sigma'_c)$ is obtained using Figure 7.
(3) The normalized cumulative dissipation energy $U_n/{}_{n+1}\sigma'_c$ at the end of n-th cycle is calculated from Eq. 12.
(4) From the normalized cumulative dissipation energy $U_n/{}_{n+1}\sigma'_c$, the maximum excess pore water pressure ratio $\Delta u_n/\sigma'_c$ is determined using Figure 6, and the excess pore water pressure ratio at the end is determined using Figure 8 to calculate the effective confining pressure ${}_{n+1}\sigma'_c$ at the next cycle.
(5) The procedures from (2) to (4) are repeated until a prescribed excess pore water pressure ratio is induced, and the number of cycles is counted against an arbitrary cyclic stress ratio. As a result, a liquefaction strength curve is obtained.

To use the relationships in Figures 6 to 8, linear interpolation was adopted to obtain values between data, and in the case where data were varied as shown in Figure 7, linear interpolation was performed after taking a running average. The number of cycles was calculated in 0.01 steps for the range of the cyclic stress ratio from 0.05 to 2.00. Therefore, the cyclic stress ratio was gradually increased from 0.035 in the tests to accurately calculate the number of cycles for the cyclic stress ratio more than 0.05.

The liquefaction strength curves calculated by the above procedure is shown in Figure 10. The liquefaction strengths for RL_{20} in GP-10-1 and GP-10-2 are 0.520 and 0.355 respectively. They are very different if the specimen were collected from the almost same depth. In other words, a conventional liquefaction strength test in that plural test pieces must be prepared, is assumed to be intensively influenced by the combination of specimens and cyclic stress ratio. Focusing the shape of the liquefaction strength curve, the rise of the liquefaction strength curve was large when the number of cycles was 10 or less. This

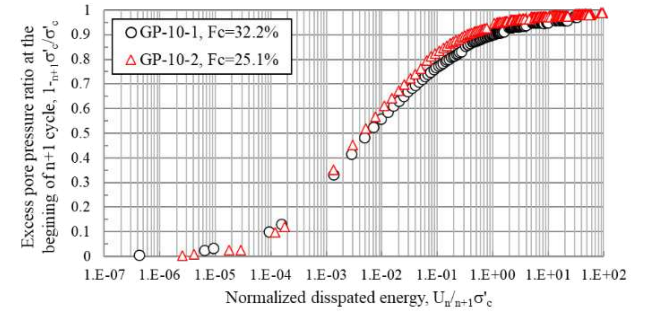behavior might be due to aging effects observed in old sedimentary ground.

Figure 8. Relationships of normalized dissipation energy and excess pore pressure ratio at the beginning of next cycle.
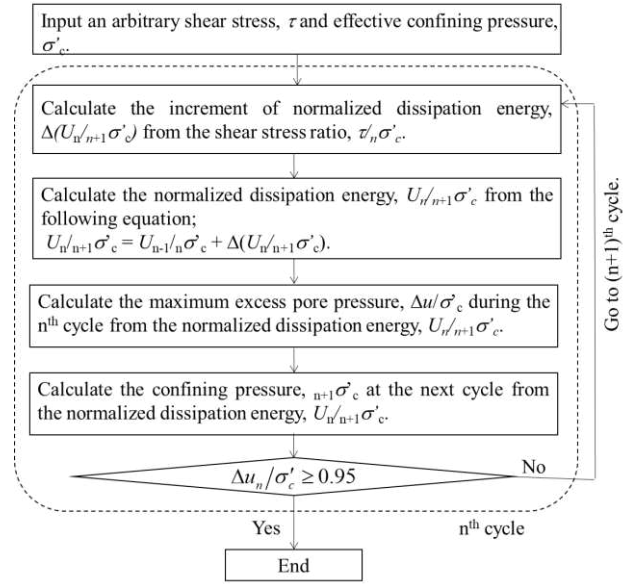

Figure 9. Flow chart to calculation liquefaction strength curve using one undrained cyclic triaxial test.
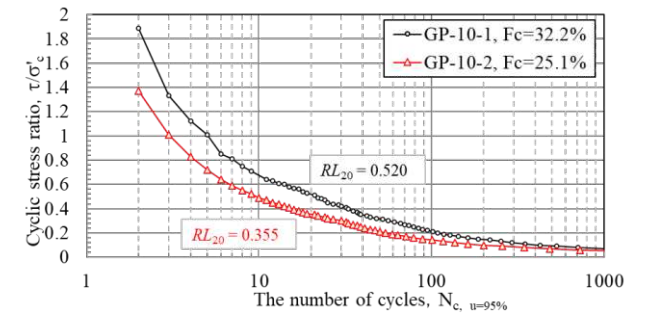

Figure 10. Estimated liquefaction strength curves from each undrained cyclic triaxial test.

4 DYNAMIC PROPERTY DURING LIQUEFACTION

It is difficult to directly compare the stress-strain relationship in laboratory tests with a result of seismic response analysis when the liquefaction analysis using effective stress is performed. To evaluate the dynamic properties of soil during liquefaction strength tests, the relationships of the excess pore water pressure ratio, equivalent shear modulus and damping ratio against the shear strain were drawn in Figures 11 to 13. In the cyclic triaxial tests, the neutral axis in a stress-strain loop moves to the extension side as shown in Figures 14 and 15, because the slope

of failure line is different between the compression and extension side as in Figures 4 and 5. Accordingly, the horizontal axis in Figures 11 to 13 indicates the single amplitude of shear strain with a half of double amplitude of shear strain.
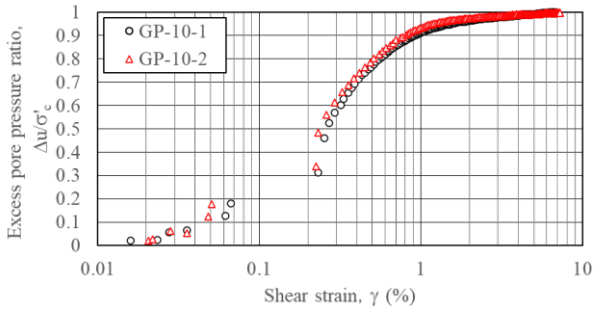

Figure 11. Relationship between shear strain and excess pore water pressure ratio.
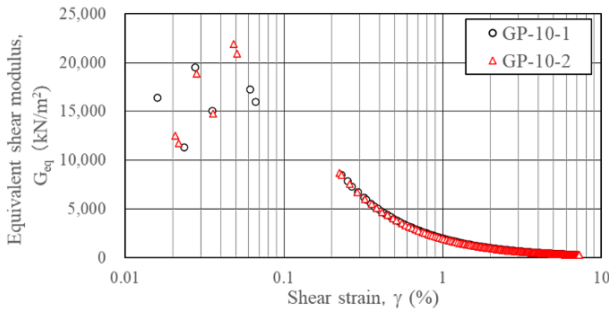

Figure 12. Relationship between shear stress and equivalent shear modulus.
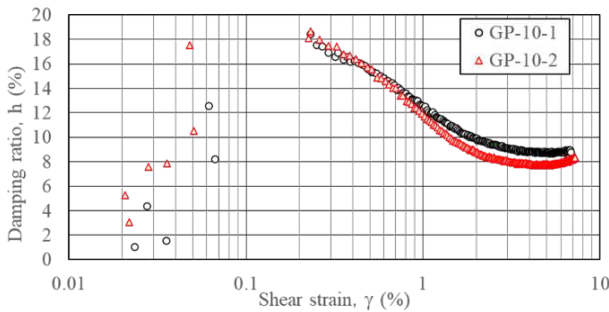

Figure 13. Relationships between shear strain and damping ratio.

From the relationship of the excess pore water pressure ratio and the shear strain in Figure 11, the brittle liquefaction did not occur. The shear strain and the excess pore water pressure gradually increased with the increase of loading cycle. The excess pore water pressure ratio of 0.95, which is thought to be initial liquefaction, was induced at a shear strain of around 1.5 %. The shear strain was larger than that of clean sand.

The initial shear modulus measured by S-wave velocity in the triaxial cell were 9.55×10^4 kN/m^2 and 7.60×10^4 kN/m^2 for GP-10-1 and GP-10-2 respectively. In Figure 12, the equivalent shear modulus was largely varied in a range of shear strain less than 0.2 %, because the small cyclic stress ratio was used up to the 6th cycle and the axial strain was measured by an external displacement transducer. Looking at the equivalent shear modulus at a shear strain of 0.2% that the values began to stabilize, the values decreased to about 1/10 of the initial shear modulus. The shear modulus at the shear strain of 0.2 % was about half or one-third of the equivalent shear modulus considering two effects; one was the rise in excess pore water pressure, the other was a typical G-γ relationship for sand. On the

other hand, the damping ratio in Figure 13 was as high as 18% at a shear strain of 0.2%, which is about twice as large as that in a typical h-γ relationship for sand. After that, the damping ratio decreased due to the progress of liquefaction.

As described above, the specimens subjected to aging effects did not induce a sudden liquefaction even if the N-value is as low as about 10. The dynamic properties measured from stress-strain loops were different from those in a usual dynamic deformation test. It suggests that a special tuning for constitutive rules is necessary to reproduce liquefaction behavior of the soil subjected to the aging effect.
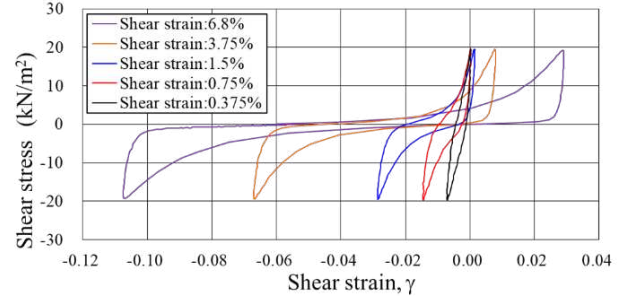

Figure 14. Loops of shear stress and shear strain in several stages for GP-10-1.
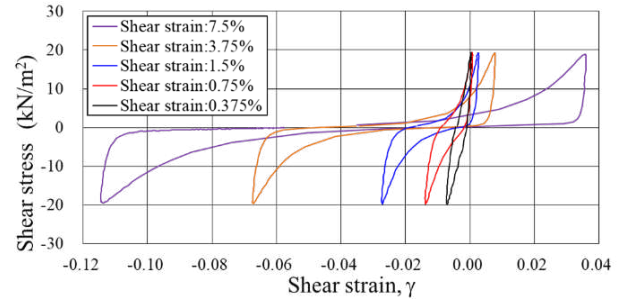

Figure 15. Loops of shear stress and shear strain in several stages for GP-10-2.

5 CONCLUSIONS

In this paper, high-quality undisturbed samples of sand with gravel were collected from Pleistocene layer with a low N-value of about 10, and undrained cyclic triaxial tests were carried out to gain the liquefaction strength curves using the concept of cumulative dissipation energy. The following conclusions were obtained.

1) The failure and phase lines for cohesive sandy soil were derived from Mohr-Coulomb's failure criteria and the relationship of p-q in triaxial tests. It was found from the stress paths that the sand with fines and gravel had small cohesion and a friction angle from 44 to 47 degrees. The friction angles were thought to be very large, though the N-value was as low as about 10.
2) The remarkable characteristic for the Pleistocene layer was a very low phase angle of 5 degrees. As a result, the specimens showed intensive cyclic mobility.
3) The liquefaction strength for RL_{20} was different between 0.355 and 0.520 even if the specimens were collected from the almost same depth. Therefore, the method of calculating the liquefaction strength curve from one specimen has the superiority for the natural sedimentary ground.
4) By receiving aging effects, the rise of liquefaction strength curve at the cyclic number of 10 times or less must be increased. This trend may be able to contribute in improving the accuracy of liquefaction evaluation in the seismic response analysis.

103

5) In the relationship between shear strain and damping ratio obtained from the stress-strain loops, the damping ratio of 18% was observed at a shear strain of 0.2 %, which was twice larger than that in a usual dynamic property test. The damping ratio decreased to about 10% with the progress of liquefaction. The reason for this is that the Pleistocene layer had a low phase angle of 5 degrees and showed intensive cyclic mobility.

6 REFERENCES

Honda T., Kiyota T., Wu C. and Shigeno K. 2020. Evaluation of liquefaction strength curve using cumulative dissipation energy, *Japanese geotechnical journal*, 15（2）, 213-224 (in Japanese).

Honda T. and Shigeno, Y. 2017. Evaluation of procurement strength curves using energy disposal, *Proc. of the 19th ICSMGE, Seoul*, 1023-1026.

Tanaka T. and Yamada S. 2015. S-wave velocity under various stress conditions using Torsion Wave type Vs actuator, *Zenchiren Technical Forum 2015, Nagoya,* No. 10 (in Japanease).

Taylor M.L., Cubrinovski M. and Haycock I. 2012. Application of new 'Gel-push' sampling procedure to obtain high quality laboratory test data for advanced geotechnical analyses. *Int, Proc. 2012 NZSEE Conference*. Paper No. 123.

Towhata I., Maruyam, S., Kasuda K., Koseki J., Wakamatsu K., Kiku H., Kiyota T., Yasuda Y., Taguchi Y., Aoyama S. and Hayashida, T. 2014. Liquefaction in the Kanto region during the 2011 off the pacific coast of Tohoku earthquake, *Soils and Foundations*, 54(4), 859 -873.

Yasuda S., Harada K., Ishikawa K. and Kanemaru Y. 2012. Characteristics of liquidation in Tokyo Bay area by the 2011 Great East Japan Earthquake, *Soils and Foundations*, 52(5), 793-810.